

## Scatter-based magnetic resonance elastography

Sebastian Papazoglou<sup>1,4</sup>, Chao Xu<sup>1,4</sup>, Uwe Hamhaber<sup>3</sup>,  
Eberhard Siebert<sup>2</sup>, Georg Bohner<sup>2</sup>, Randolph Klingebiel<sup>2</sup>,  
Jürgen Braun<sup>3</sup> and Ingolf Sack<sup>1,5</sup>

<sup>1</sup> Department of Radiology, Charité—Universitätsmedizin Berlin, Campus Mitte, Charitéplatz 1, 10117 Berlin, Germany

<sup>2</sup> Department of Neuroradiology, Charité—Universitätsmedizin Berlin, Campus Mitte, Charitéplatz 1, 10117 Berlin, Germany

<sup>3</sup> Institute of Medical Informatics, Charité—Universitätsmedizin Berlin, Campus Benjamin Franklin, Hindenburgdamm 30, 12200 Berlin, Germany

E-mail: [ingolf.sack@charite.de](mailto:ingolf.sack@charite.de)

Received 16 October 2008, in final form 28 January 2009

Published 17 March 2009

Online at [stacks.iop.org/PMB/54/2229](http://stacks.iop.org/PMB/54/2229)

### Abstract

Elasticity is a sensitive measure of the microstructural constitution of soft biological tissues and increasingly used in diagnostic imaging. Magnetic resonance elastography (MRE) uniquely allows *in vivo* measurement of the shear elasticity of brain tissue. However, the spatial resolution of MRE is inherently limited as the transformation of shear wave patterns into elasticity maps requires the solution of inverse problems. Therefore, an MRE method is introduced that avoids inversion and instead exploits shear wave scattering at elastic interfaces between anatomical regions of different shear compliance. This compliance-weighted imaging (CWI) method can be used to evaluate the mechanical consistency of cerebral lesions or to measure relative stiffness differences between anatomical subregions of the brain. It is demonstrated that CWI-MRE is sensitive enough to reveal significant elasticity variations within inner brain parenchyma: the caudate nucleus (head) was stiffer than the lentiform nucleus and the thalamus by factors of  $1.3 \pm 0.1$  and  $1.7 \pm 0.2$ , respectively ( $P < 0.001$ ). CWI-MRE provides a unique method for characterizing brain tissue by identifying local stiffness variations.

### Introduction

Examination of the body with the hands remains an elementary diagnostic procedure despite the enormous progress of modern medical imaging techniques. The physical quantity the physician examines by palpation is the shear modulus, which describes the response of

<sup>4</sup> Contributed equally to this paper.

<sup>5</sup> Author to whom any correspondence should be addressed.

incompressible materials to shear strain. The shear modulus of human tissues varies over several orders of magnitude (Sarvazyan *et al* 1995) and is highly sensitive to pathologic tissue alterations (Samani *et al* 2007). Magnetic resonance elastography (MRE) is a noninvasive imaging technique that exploits the shear modulus to distinguish different soft tissues (Plewes *et al* 1995, Muthupillai and Ehman 1996). The classic MRE experiment consists of three parts: shear wave stimulation, wave image acquisition using motion-sensitive MRI and calculation of elastograms by wave field inversion. To date, these principles have been most successfully applied for diagnosing liver fibrosis taking into account global viscoelastic constants of the entire organ (Yin *et al* 2007, Asbach *et al* 2008, Huwart *et al* 2008). In contrast, the measurement of locally resolved mechanical parameters is still a challenge since the calculation of elastograms encounters ill-posed inverse problems due to noise, unknown boundary conditions and uncertain shear wave sources (Papazoglou *et al* 2008). Against this background a stiffness-weighted MRE method was recently developed by Glaser *et al* (2006) based on cyclic MRI signal attenuation due to intravoxel phase dispersion (IVPD) (Glaser *et al* 2003), which does not require the solution of an inverse problem. As IVPD depends on the local phase gradient of the shear waves, high wave amplitudes with short wavelengths corresponding to high drive frequencies are desired in this approach. Here we introduce a method which reversely exploits low-frequency oscillations, giving rise to large wavelengths extending even beyond the investigated organ. As a technical consequence, shear wave damping through viscosity is reduced to negligibility, which allows applying smaller vibration amplitudes than would be required when using high excitation frequencies ( $f$ ). Additionally, the intensity of the shear waves—which is the crucial parameter for safety considerations in MRE (Ehman *et al* 2008)—is considerably reduced at low frequencies as it scales with  $f^2$ . Thus, MRE of mechanically vulnerable organs such as the brain would benefit most from low-drive frequency techniques. In the following, an MRE method is introduced that utilizes very low frequency vibrations (10 Hz) and that does not rely on wave inversion for obtaining spatially resolved elasticity information. Since the image contrast produced in this way is scaled by the inverse stiffness of the tissue, the proposed method is accordingly termed compliance-weighted imaging (CWI).

In the following, a model of shear wave scattering by cylindrical inclusions is employed as the basic theoretical concept of CWI. After a brief analytical description of the shear strain signal in scatter-based MRE, we present the CWI method and show its feasibility in simulations and experiments on a phantom and *in vivo* brain. To demonstrate its reproducibility, CWI is applied to measure relative stiffness differences of subcortical gray matter in 12 healthy volunteers, which is known to be involved in several psychiatric and neurological diseases. For Alzheimer's disease (Rombouts *et al* 2000), multiple sclerosis (Bakshi *et al* 2002), Sydenham's chorea (Ikuta *et al* 1998), Creutzfeldt-Jakob disease (Dirocco *et al* 1993, Schroter *et al* 2000) as well as schizophrenia (Shenton *et al* 2001), abnormal hyper- or hypointense MRI signals have been reported or volume changes on MRI images were found in the basal ganglia or the thalamus. The evaluation of their elasticity may provide useful information for early diagnosis of related diseases. Finally, it will be demonstrated in a patient with subcortical cerebral metastasis that CWI-MRE is feasible and can be used to assess the consistency of tumors prior to an intervention.

## Theory

To elaborate on the origin of contrast in compliance-weighted MRE, we regard the measured strain field as a result of shear wave scattering by elastic inclusions. In this section, the principles of plane shear wave scattering are derived from a simple geometrical setting based

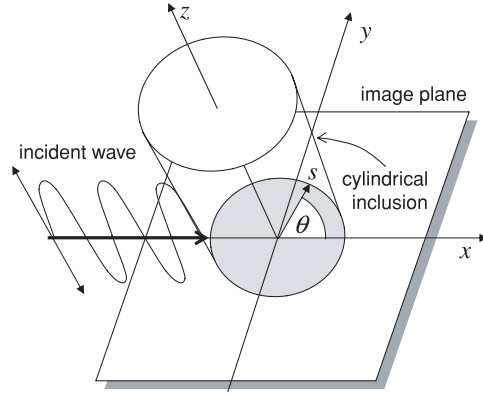


**Figure 1.** Coordinates and inclusion model used to analyze shear-horizontal (SH) wave scattering in MRE.

on an elastic cylinder with radius  $R$  embedded in an infinite elastic matrix. Polarization of the waves shall be through plane (in the  $z$ -direction within an  $x$ - $y$  imaging plane) as it is the preferred polarization direction in planar MRE (Papazoglou *et al* 2008, Yin *et al* 2008). To approach this condition in brain MRE experiments, a head vibrator was utilized that mainly induced a nodding motion of the head perpendicular to the axial imaging plane (Sack *et al* 2008). Henceforth, this major field component ( $u$ ) will be subjected to shear-horizontal wave scattering by the inclusion located at the origin of our cylindrical coordinate system ( $s, \theta, z$ ) (figure 1). This scattering scenario is solved using the eigenfunction expansion known from the literature (Graff 1991). The scalar field  $u(s, \theta, \omega)$  is decomposed into the incident plane wave with the amplitude  $u_0$ , the scattered field  $u^{\text{sca}}$  and the refracted field  $u^{\text{ref}}$ :

$$u(s, \theta, \omega) = u_0 \exp(i\mathbf{k}_1 \mathbf{r}) + u^{\text{sca}}(s, \theta, \omega) + u^{\text{ref}}(s, \theta, \omega), \quad (1)$$

where  $|\mathbf{k}_1| = k_1 = \omega/c_1$  is the wave number in the matrix with  $c_1$  as the phase velocity and  $\omega = 2\pi f$ . The refracted field can be expressed as the series

$$u^{\text{ref}}(s, \theta, \omega) = \sum_{n=-\infty}^{\infty} a_n J_n(k_2 r) \exp(in\theta), \quad (2)$$

with  $J_n$  being the Bessel function of the first kind of order  $n$  and  $k_2$  the wave number inside the inclusion ( $|\mathbf{k}_2| = k_2 = \omega/c_2$ , with the phase velocity of the scatterer  $c_2$ ). A unit density of  $\rho = 1 \text{ kg l}^{-1}$  is assumed for all compartments in the material. The expansion coefficients  $a_n$  are determined by the boundary conditions, i.e. by requiring continuity of displacement and traction across the surface of the cylinder. They read

$$a_n = \frac{c_1 [J_n(k_1 R) H_n'(k_1 R) - J_n'(k_1 R) H_n(k_1 R)]}{c_1 J_n(k_2 R) H_n'(k_1 R) - c_2 J_n'(k_2 R) H_n(k_1 R)}, \quad (3)$$

where  $H_n$  is the Hankel function of the first kind of order  $n$  and the prime denotes the derivative with respect to the argument. The only non-zero components of the strain inside the inclusion are

$$\varepsilon_{zs}^{\text{ref}} = \frac{1}{2} \frac{\partial u^{\text{ref}}}{\partial s}, \quad \varepsilon_{z\theta}^{\text{ref}} = \frac{1}{2s} \frac{\partial u^{\text{ref}}}{\partial \theta}. \quad (4)$$

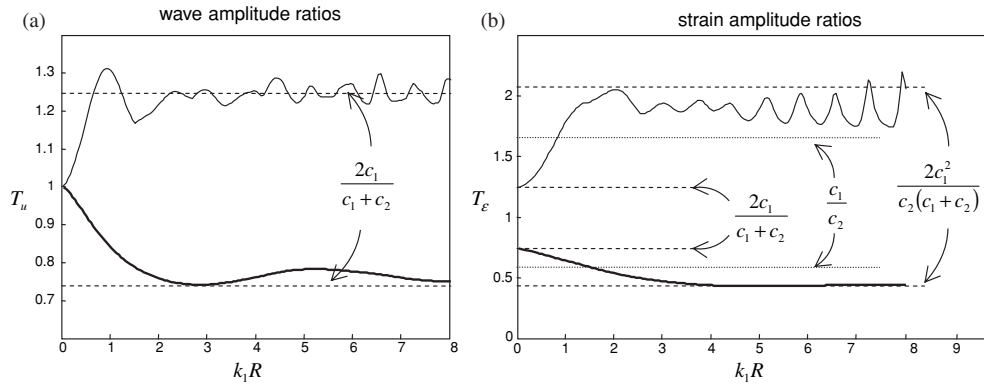


**Figure 2.** SH wave scattering by a cylindrical inclusion of radius  $R$  embedded in an elastic matrix. Transmission coefficients of shear wave amplitudes  $T_u$  (a) and shear strain  $T_\varepsilon$  (b) shown for two different elastic scenarios: inclusion stiffness 4 kPa (thin solid line) and 32 kPa (fat solid line); matrix stiffness 11 kPa in both cases. The indices 1 and 2 for wave speed  $c$  and wave number  $k$  refer to matrix and inclusion, respectively. Simulations were performed by numerically integrating equation (5).

To estimate the degree of scattering, we will further account for the averaged absolute values of amplitudes and strains:

$$\begin{aligned}\bar{u}^{\text{ref}} &= \frac{1}{2\pi R} \int_0^R \int_0^{2\pi} |u^{\text{ref}}| \, ds \, d\theta, \\ \bar{\varepsilon}^{\text{ref}} &= \frac{1}{2\pi R} \int_0^R \int_0^{2\pi} |\varepsilon_{zs}^{\text{ref}}| + |\varepsilon_{z\theta}^{\text{ref}}| \, ds \, d\theta.\end{aligned}\quad (5)$$

These functions are normalized with the incident wave of amplitude  $u_0$ , yielding the transmission coefficients for amplitudes and strain:

$$T_u = \frac{\bar{u}^{\text{ref}}}{u_0} \quad \text{and} \quad T_\varepsilon = \frac{\bar{\varepsilon}^{\text{ref}}}{u_0 k_1}.\quad (6)$$

In the limit of  $\omega \rightarrow \infty$ ,  $T_u$  approaches the well-known transmission coefficient of a plane shear-horizontal wave normally incident to an infinite plane interface (Papazoglou *et al* 2007) whereas in the regime of Rayleigh scattering ( $k_1 R \ll 1$ ),  $T_u$  approaches 1 (figure 2(a)):

$$\begin{aligned}T_u &\rightarrow 1 && \text{for } \omega \rightarrow 0 \\ T_u &\rightarrow \frac{2c_1}{c_1 + c_2} && \text{for } \omega \rightarrow \infty.\end{aligned}\quad (7)$$

Thus, at low drive frequencies, the amplitudes of scattered shear waves are insensitive to elastic interfaces. This is in contrast to the strain, which conveys elastic information also at low frequencies. The low- and high-frequency limits of  $T_\varepsilon$  are given by

$$\begin{aligned}T_\varepsilon &\rightarrow \frac{2c_1}{c_1 + c_2} && \text{for } \omega \rightarrow 0, \\ T_\varepsilon &\rightarrow \frac{2c_1^2}{c_2(c_1 + c_2)} && \text{for } \omega \rightarrow \infty.\end{aligned}\quad (8)$$

Interestingly, both limits are related to the transmission coefficient of the plane interface model  $T_u = 2c_1/(c_1 + c_2)$  by  $\bar{\varepsilon}^{\text{ref}}(\omega \rightarrow 0) = u_0 T_u \cdot k_1$  and  $\bar{\varepsilon}^{\text{ref}}(\omega \rightarrow \infty) = u_0 T_u \cdot k_2$ . Thus, in the

limit of Rayleigh scattering at low  $\omega$ , the sensitivity of  $T_\varepsilon$  to the change of elastic properties is diluted by the matrix property  $k_1$ . In the regime of Mie scattering ( $k_1 R \geq 1$ ) an increasing influence of inclusion property  $k_2$  causes an increase in the strain transmission coefficient. For estimating the regime of scattering in our *in vivo* experiments, we use  $c_1 = 0.9 \text{ m s}^{-1}$  wave speed in brain matter at 10 Hz according to an interpolation of experimental data of a higher frequency range given in Klatt *et al* (2007). This yields  $k_1 R = 0.7$  to 1.4 for inclusion diameters between 1.0 and 2.0 cm. Thus, *a priori* knowledge of inclusion size and matrix elasticity is required in order to estimate correct stiffness ratios in scatter-based elastography. As this is not feasible in a clinical setting, simplification is required, which we gain by accounting for the mean value of both limits of  $T_\varepsilon$  (see equation (8) and figure 2(b)):

$$\frac{T_\varepsilon(\omega \rightarrow 0) + T_\varepsilon(\omega \rightarrow \infty)}{2} = \frac{c_1}{c_2}. \quad (9)$$

This wave speed ratio between compartments 1 and 2 equals the inverse ratio of the averaged strains. Using equation (6) and the relation  $k_1 = \omega/c_1$ , equation (9) can be expressed in terms of the shear modulus  $\mu$  inside the inclusion:

$$(\bar{\varepsilon}^{\text{ref}})^2 = \rho \frac{u_0^2 \omega^2}{\mu}. \quad (10)$$

The proportionality of squared strain to tissue compliance ( $\varepsilon^2 \sim 1/\mu$ ) is henceforth utilized to assess tissue's mechanical properties. It is important to note that equation (10) applies to a matrix not only with a single inclusion but also in case of two inclusions (correspondingly indexed by 1 and 2) that are embedded in the same material:

$$\left(\frac{\varepsilon_1}{\varepsilon_2}\right)^2 = \frac{\mu_2}{\mu_1}. \quad (11)$$

Extending this idea toward a scatter-based image contrast, we assume a uniform tissue matrix with an arbitrary number of scatterers. Then, the matrix strain is regarded as the background signal while the strain inside the scatterers represents a correlate of tissue compliance which implies the aforementioned assumptions of uniform mass density and  $kR \sim 1$ . Figure 2(b) indicates that the deviation from these assumptions causes a variation in strain sensitivity with respect to  $1/c$ . However, regardless of specific wave numbers and inclusion diameters, stiff regions will always appear darker in  $\varepsilon^2$  maps than soft regions, suggesting that our approach displays the compliance-weighted image contrast of a tissue.

#### Generation of compliance-weighted images from MRI phase images

Phase unwrapping is usually required in processing phase-sensitive MRI data for extending the range of the phase signal  $\phi \in [0, 2\pi]$ . Since strain images are generated in CWI, the uncertainty of 2D unwrapping algorithms can be avoided by directly deriving  $\partial\phi/\partial x$  and  $\partial\phi/\partial y$  from the wrapped phase signal:

$$\frac{\partial\phi}{\partial(x, y)} = -i \exp(-i\phi) \frac{\partial}{\partial(x, y)} \exp(i\phi). \quad (12)$$

The resulting derivatives are converted to CWI contrast employing the parameter of the 'efficiency of motion encoding' as introduced in Asbach *et al* (2008):

$$C = \left| \frac{\pi(1 - \tau^2 f^2)}{\gamma g \tau \sin(\pi N \tau f)} \right| \left( \left[ \frac{\partial\phi}{\partial x} \right]^2 + \left[ \frac{\partial\phi}{\partial y} \right]^2 \right). \quad (13)$$

This equation applies to harmonic motions encoded by a sinusoidal motion-encoding gradient (MEG) of amplitude  $g$ , period time  $\tau$  and number of gradient periods  $N$  (Rump *et al* 2007).

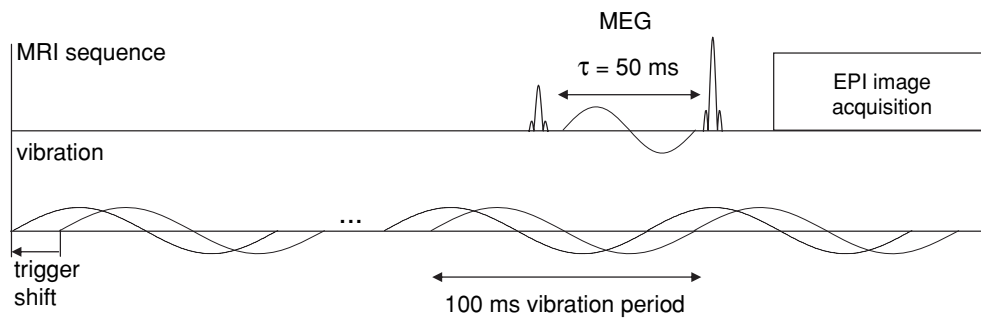


**Figure 3.** Diagram of motion and sequence timing in CWI-MRE using a single-shot spin-echo EPI sequence.

$\gamma$  is the gyromagnetic ratio of the protons. The complex-valued wave used in our model is experimentally mimicked by acquiring several phase images  $\phi$  at multiple delays between motion and MEG. Such dynamic scans of  $C$  display propagating oscillation patterns whose time average over a vibration period corresponds to  $\varepsilon^2 \sim 1/\mu$ . In the following, the time average  $\langle C \rangle$ , i.e. the expectation value of  $C$ , is termed CWI contrast.  $\langle C \rangle$  may still display oscillation patterns as a result of insufficient  $\phi$ -cycling in combination with boundary effects. Such shallow variations of the CWI background can be suppressed by appropriate band-reject filters.

## Methods

An agarose cube (1.0 w%) measuring  $10 \times 12 \times 10 \text{ cm}^3$  was used as a matrix for three cylindrical inclusions ( $\phi$  1.5 cm) of 1.5, 0.75 and 0.5 w% agarose. Unlike in brain experiments, a vibration frequency of 50 Hz was used as the elasticity of the gel matrix was much higher than the elasticity of *in vivo* brain parenchyma (about six-fold higher compared to data given in Klatt *et al* (2007)). A head cradle attached to a remote vibration generator (Sack *et al* 2008) was used for exciting 10 Hz intracranial shear oscillations applying repeated bursts of four sinusoidal cycles. *In vivo* examinations were performed on 12 healthy volunteers without overt neurological or psychiatric conditions (mean age 31 years; age range 22–38 years; seven males and five females) and one patient with renal cell carcinoma and cerebral metastasis of approximately 12 mm diameter located in the left rolandic region of the anterior parietal lobe. Institutional review board approval and written informed consent were obtained.

### Wave image acquisition

All examinations were performed on a 1.5 T scanner (Magnetom Sonata; Siemens, Erlangen, Germany) using a standard head coil. A single-shot spin-echo echo-planar imaging (EPI) sequence was sensitized to motions in variable directions by a sinusoidal motion-encoding gradient (MEG) with amplitude  $g = 35 \text{ mT m}^{-1}$ . The phantom experiment was performed with  $N = 2$ ,  $\tau = 20 \text{ ms}$ ,  $f = 50 \text{ Hz}$ . Head vibrations of 10 Hz were encoded by  $N = 1$  and  $\tau = 50 \text{ ms}$ . A trigger signal was given to the wave generator at the beginning of every second image acquisition for consecutively measuring vibration and no-vibration data. As shown in figure 3, the trigger shift between wave burst and MEG was increased 20 times by an increment of  $1/(20 \cdot f)$  in the phantom and patient studies and 40 times by an increment of  $1/(40 \cdot f)$  in the volunteer examinations. Further image acquisition parameters were transverse slice position;

repetition time 3 s; echo time 124 s; field of view  $192 \times 192$  mm; slice thickness 6 mm; in-plane-resolution  $1.5 \times 1.5$  mm. Total scan time was 2 min in the patient study and 4 min in the volunteer examinations.

#### *Numerical simulation and data analysis*

Horizontal shear wave scattering at multiple cylindrical inclusions was simulated employing the method of Biwa *et al* (2004) with geometry of matrix and scatterers adopted from the experimental setup. The simulations were run using elastic values for the matrix of 11 kPa and for the inclusions of 32, 8 and 4 kPa. These parameters were determined from MRE at a higher drive frequency ( $f = 200$  Hz) utilizing the slope of wavefronts (regions of a constant wave phase) along selected profiles similar to the method described in Papazoglou *et al* (2006). Phase images  $\phi(t)$  were treated according to equations (12) and (13), resulting in a series of time-resolved  $C(t)$  images, which were averaged to  $\langle C \rangle$ . A Butterworth band-reject filter  $F = 1 / (1 + [k \cdot W / (k^2 - k_0^2)]^4)$  with a width of  $W = 67 \text{ m}^{-1}$  and a central band position of  $k_0 = 13 \text{ m}^{-1}$  was used for the display of *in vivo* CWI maps. Subcortical gray matter was segmented into the caudate nucleus, the lentiform nucleus and the thalamus. Further distinction of subregions such as the putamen and pallidum was not possible due to the limited spatial resolution of the MRE scans (voxel size of  $1.5 \times 1.5 \times 6 \text{ mm}^3$ ). Segmentation was performed by means of averaged magnitude contrast images acquired synchronously to the MRE phase images and compared with T2-weighted spin echo images.

## **Results**

#### *Simulation and phantom study*

Figure 4 demonstrates principles of CWI-MRE by simulations and experiments. The elastic parameters used in simulations suggest stiffness ratios  $R_1 = 0.34$ ,  $R_2 = 1.37$  and  $R_3 = 2.75$  of stiff (32 kPa), medium (8 kPa) and soft (4 kPa) inclusions relative to the matrix (11 kPa). CWI applied to simulated data yielded the ratios  $R_1 = 0.48 \pm 0.15$ ,  $R_2 = 1.32 \pm 0.37$  and  $R_3 = 2.88 \pm 0.89$ . The error margins correspond to the standard deviation of  $\langle C \rangle$  within the region of interest (ROI), where residues of the shear waves cause a variation of  $\langle C \rangle$ . Comparison with the experiments shows an enhancement of wave residues due to reflecting vessel walls (which were not accounted for in the simulations). Deterioration of CWI intensity inside the soft and medium inclusions can possibly be attributed to wave damping or negative wave interferences. Stiffness ratios were deduced from the CWI map shown in figure 4(d) with  $R_1 = 0.65 \pm 0.28$ ,  $R_2 = 1.62 \pm 0.90$  and  $R_3 = 3.71 \pm 2.26$ .

#### *Volunteer and patient studies*

Figure 5 demonstrates *in vivo* CWI-MRE of the brain in a transverse slice through the corpus callosum. A standard T2-weighted (T2w) MR image acquired in the same slice position is shown for comparison. Phase difference wave data are displayed for different motion-encoding directions. In-plane motion components show a constant slope of the spin phase from right to left and from top to bottom corresponding to the chosen MEG directions. Therefore, the calculation of  $\langle C \rangle$  yields a uniform image contrast indicating that no elastic in-plane strain-wave is produced by our actuator. Instead, rigid motion of the entire brain is seen in figures 5(a) and (b) which cannot produce a scatter-based image contrast aside of some intensity due to cerebrospinal fluid (CSF). In contrast, the through-plane deflection component

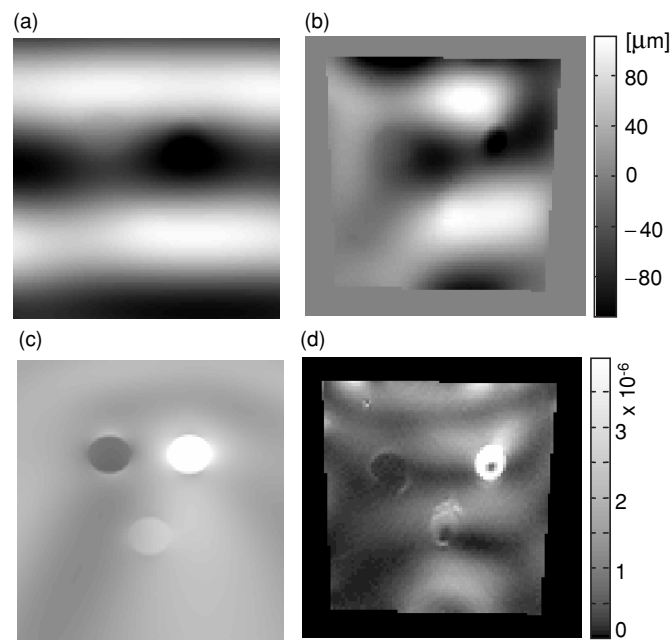


**Figure 4.** (a) Simulation of a 50 Hz shear wave scattered at three cylindrical inclusions of different stiffness using the method of Biwa *et al* (2004) (the real part of the complex wave is shown). (b) Experimental 50 Hz shear wave in a heterogeneous phantom with three cylindrical inclusions. (c), (d) Compliance weight ( $C$ ) of the simulation and the experiment shown above.

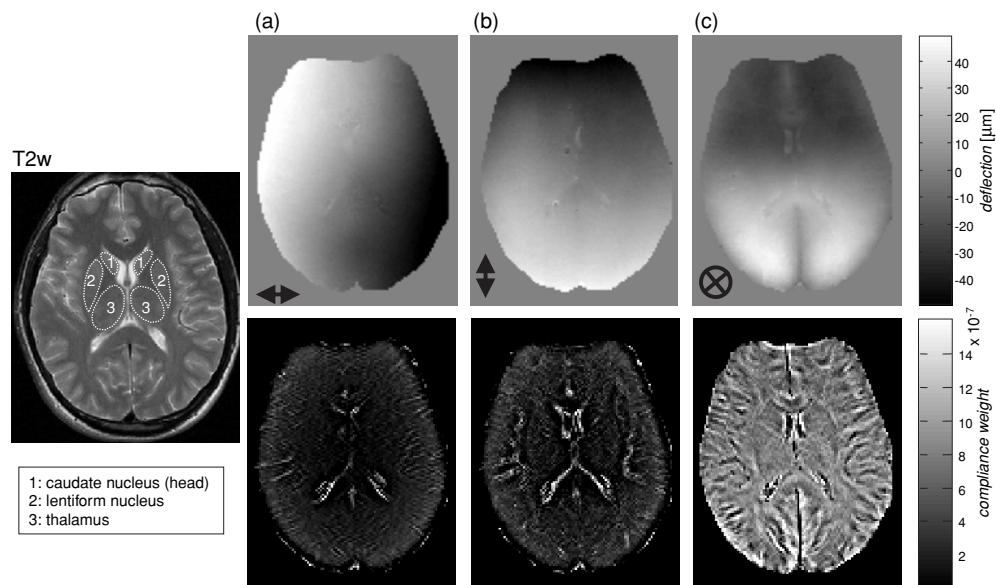


**Figure 5.** Brain CWI-MRE in a healthy volunteer. The standard T2-weighted (T2w) image contrast is given on the left-hand side. Unwrapped wave images are shown in the upper row of (a), (b) and (c) while the bottom row represents CWI contrast according to equations (12) and (13). The direction of motion sensitization was (a) left-right, (b) top-bottom and (c) through plane. The regions demarcated in the T2w image were further analyzed for relative compliance in 12 healthy volunteers.

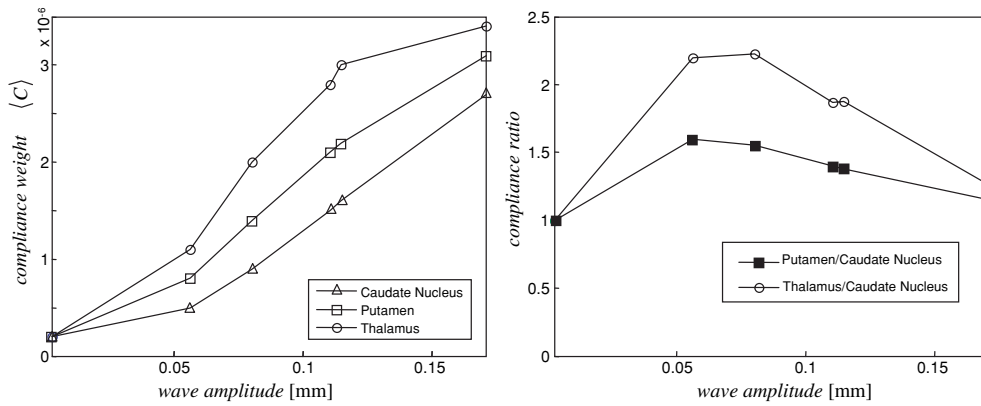


**Figure 6.** Compliance weights (left) and compliance ratios (right) for different amplitudes of the induced cerebral shear waves.

is governed by elastic strain giving rise to significant CWI intensity. The image in figure 5(c) (bottom line) results from the mechanical heterogeneity of the brain corresponding to its anatomical structure: basal ganglia, thalamus, genu and splenium of the corpus callosum are well distinguishable from the internal capsule. The CWI contrast inside sulci and ventricles is due to the fluid dynamics of CSF yielding arbitrary amplitude variations during head vibration.

The influence of the drive amplitude on  $\langle C \rangle$  is demonstrated in figure 6. As already seen in figure 5, the information in CWI is bound to elastic strain. Therefore, the  $\langle C \rangle$  intensity at low drive amplitudes represents pure noise whereas significant wave deflection results in a compliance-weighted contrast given by increasing  $\langle C \rangle$  values. At a certain level of vibration amplitudes, the phase signal is destroyed by IVPD, causing a loss of information in CWI. This is well demonstrated in the right panel of figure 6, where stiffness ratios between the lentiform nucleus and the caudate nucleus ( $R_a$ ) and the thalamus and the caudate nucleus ( $R_b$ ) display a maximum around deflections of  $60 \mu\text{m}$ . Henceforth, this desired range of wave amplitudes was exploited for investigating interindividual stiffness variations within subcortical gray matter. The observation of through-plane IVPD in figure 6 implies that the derivative  $\partial u / \partial z$  is not zero, which we attribute to diffraction due to the vicinity of the extended wave source given by skull and meninges. Such realistic wave properties inside the brain clearly limit the used plane wave approach. On the other hand, a full 3D-tensor field acquisition with sufficient through-plane resolution is not yet feasible in a clinical setting of brain MRE.

Table 1 lists  $\langle C \rangle$  values corresponding to the ROIs indicated in figure 5. In both hemispheres of each volunteer, the compliance decreased in the order of thalamus > lentiform nucleus > caudate nucleus (except for the left hemisphere in volunteer 11). A  $t$ -test (paired samples, two-tailed) revealed statistical significance with  $P$ -values  $< 10^{-8}$ . The caudate nucleus with the highest relative stiffness values was used for normalizing stiffness ratios.  $R_a$  (lentiform nucleus/caudate nucleus) and  $R_b$  (thalamus/caudate nucleus) were measured with  $1.27 \pm 0.11$  and  $1.66 \pm 0.21$ . Similar ratios are obtained by applying the band-reject filter given in the Methods section:  $R_a = 1.40 \pm 0.38$  and  $R_b = 1.64 \pm 0.35$ . Despite the higher interindividual standard deviation caused by filtering,  $R_b$  remains significantly higher than  $R_a$  ( $P < 10^{-7}$ ).  $\langle C \rangle$  values for the caudate nucleus appear to be systematically higher for the left than for the right hemisphere ( $P = 0.027$ ). This trend may be due to a systematic disparity of motion amplitudes between both hemispheres possibly caused by an asymmetric wave actuation of our cradle device.

**Table 1.**  $\langle C \rangle$  values and ratios measured in three anatomical regions of both cerebral hemispheres (L: left, R: right) of 12 volunteers.  $R_a$  and  $R_b$  refer to the lentiform nucleus to caudate nucleus ratio and thalamus to caudate nucleus ratio, respectively. Mean values are given with a range of confidence ( $\pm$ ) at  $\alpha = 0.01$ .

Volunteer	Hemisphere	Compliance weight $\langle C \rangle$ ( $\times 10^{-6}$ )			Ratio	
		Caudate nucleus (head)	Lentiform nucleus	Thalamus	$R_a$	$R_b$
1	L	2.01	2.54	2.81	1.26	1.39
	R	2.24	2.65	2.80	1.18	1.25
2	L	2.66	3.56	4.01	1.34	1.50
	R	2.49	3.49	3.92	1.40	1.58
3	L	1.30	1.53	2.29	1.17	1.76
	R	1.49	1.78	2.49	1.19	1.67
4	L	1.99	3.05	3.86	1.53	1.94
	R	1.69	1.99	3.10	1.18	1.84
5	L	1.48	1.94	2.84	1.31	1.92
	R	1.31	1.54	2.37	1.17	1.80
6	L	2.01	2.66	3.26	1.32	1.62
	R	1.52	2.21	2.98	1.46	1.97
7	L	1.91	1.99	2.93	1.05	1.54
	R	1.80	2.10	2.80	1.17	1.55
8	L	2.04	2.97	3.82	1.46	1.87
	R	1.98	2.60	3.53	1.31	1.79
9	L	1.87	2.30	3.07	1.23	1.64
	R	1.42	2.06	2.83	1.46	1.99
10	L	2.30	2.97	4.04	1.29	1.76
	R	1.90	2.73	4.05	1.44	2.13
11	L	1.19	1.16	1.29	0.98	1.08
	R	0.85	1.05	1.36	1.24	1.61
12	L	2.99	3.36	3.80	1.12	1.27
	R	2.98	3.43	3.78	1.15	1.27
Mean		1.89	2.40	3.08	1.27	1.66
$\pm$		0.42	0.56	0.60	0.11	0.21

Figure 7 demonstrates the use of CWI-MRE for characterizing a histologically confirmed cerebral metastasis from a renal cell carcinoma in the left anterior parietal lobe. Standard T2w images demonstrated a cystic necrotic center and surrounding edema. The bright T2w image contrast of the peripheral edema as seen in figure 7(a) is eliminated in  $\langle C \rangle$ , indicating a similar tissue compliance of edema and surrounding brain matter. In contrast, bright CWI intensity at the edges of the metastasis suggests very soft tissue as a result of tissue degeneration. The CWI signal blank in the center of the metastasis indicates fluid-like properties, which is supported by the wavefront gradient analysis in figure 8 revealing a very low shear modulus of  $4.2 \pm 0.5$  Pa.

## Discussion

CWI-MRE was introduced to image the mechanical response of tissue to shear vibration without the need for sophisticated stiffness reconstruction algorithms including wave inversion and phase unwrapping. CWI depends on relative strain intensities that vary as a result of shear wave scattering. It is therefore particularly suited to display alterations of the mechanical constitution of tissue due to lesions. For such qualitative assessment of regional elastic

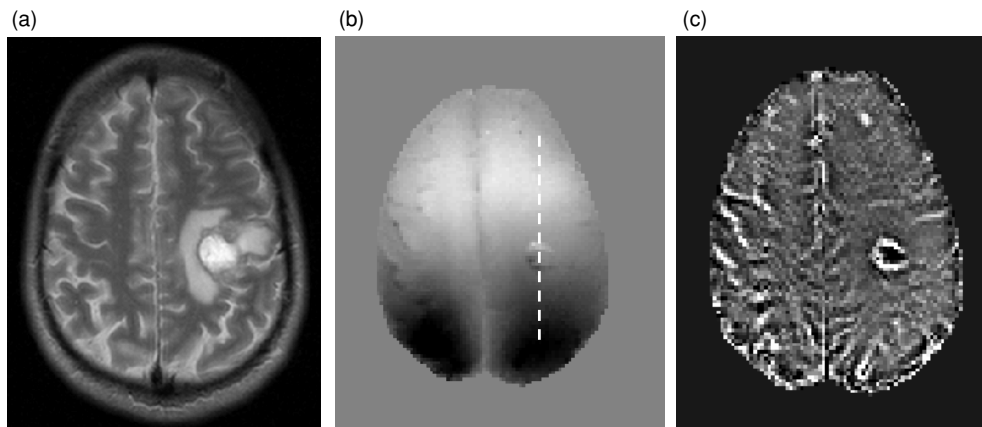


**Figure 7.** CWI-MRE on a patient with cerebral metastasis and perifocal edema. (a) T2-weighted image contrast. (b) Wave deflection image resulting from 10 Hz head vibration; the gray scale window is between  $\pm 40 \mu\text{m}$ . The dashed line demarcates the position of the profile used for the wavefront gradient analysis presented in figure 8. (c) CWI contrast indicating a high leap in acoustic impedance between edema and metastasis with strong wave damping inside the lesion.

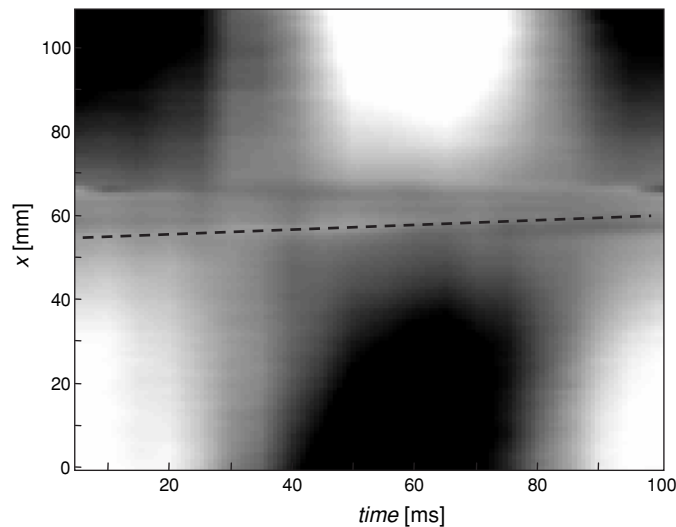


**Figure 8.** Temporal evolution of waves inside the brain along the vertical profile shown in figure 5. Propagating waves are visible inside the lesion as highlighted by the ascending dashed line whose slope corresponds to a wave speed of  $0.065 \pm 0.004 \text{ m s}^{-1}$ .

properties, CWI-MRE is not strictly bound to the proportionality  $\langle C \rangle \sim 1/\mu$ . As demonstrated by the patient study, a lesion can be characterized mechanically by the CWI signal at the site of the elastic interface where wave damping has not yet occurred. In this regard, CWI can be seen as a tool for displaying interfaces rather than quantifying stiffness ratios.

Furthermore, CWI-MRE may provide new insights into the mechanical behavior of subcortical gray matter since this region is less influenced by boundary effects than cortical regions. Applying wave inversion to brain MRE data has produced contradicting results with respect to the relative stiffness of gray and white matter (Kruse *et al* 2008, Green *et al* 2008).

The experiments presented in this study may unravel certain effects impairing wave inversion in MRE of the brain. The effects causing the CWI contrast exploited here contribute to any *in vivo* MRE experiment of heterogeneous tissue: sulci, blood vessels and elastic interfaces cause wave scattering, thereby altering shear wave amplitudes. At a certain degree of amplitude variation this may impact the analysis of the underlying shear wavelengths by inversion algorithms since steep phase changes become indistinguishable from short wavelengths. Our *in vivo* data showed no distinct change in tissue compliance at gray/white matter interfaces (see figures 5(c) and 7(c)) suggesting that elasticity differences between these regions are minimal. Sensitivity and specificity of CWI to different types of tissue and pathologies remain to be determined in future studies. These examinations need to investigate lesions of different type, size and location to draw meaningful conclusions about the clinical relevance of CWI-MRE.

In summary, scatter-based CWI-MRE was introduced to assess the elasticity of cerebral lesions in relation to surrounding healthy brain tissue. A model of cylindrical elastic inclusions was employed to deduce elasticity ratios from alterations in shear strain. The experiments clearly show the ability of CWI to resolve stiffness changes with a spatial extension far below shear wavelengths. Unlike in wave-inversion-based MRE, very low driving frequencies on the order of several hertz can be used for deriving CWI maps. This considerably improves patient acceptance of brain MRE. CWI can provide valuable information on the consistency of tumors or generally characterize the mechanical properties of small regions in the brain which are not resolved by classic MRE. Using CWI-MRE, we show for the first time that stiffness differences exist between subcortical gray matter in healthy subjects. These results set the background for future applications of CWI-MRE as a noninvasive diagnostic modality.

## Acknowledgment

This study was supported by the German Research Foundation (Sa 901/3) and the Centre for Stroke Research Berlin (BMBF 01 EO 0801).

## References

- Asbach P, Klatt D, Hamhaber U, Braun J, Somasundaram R, Hamm B and Sack I 2008 Assessment of liver viscoelasticity using multifrequency MR elastography *Magn. Reson. Med.* **60** 373–9
- Bakshi R, Benedict R H B, Bermel R A, Caruthers S D, Puli S R, Tjoa C W, Fabiano A J and Jacobs L 2002 T2 hypointensity in the deep gray matter of patients with multiple sclerosis—a quantitative magnetic resonance imaging study *Arch. Neurol.* **59** 62–8
- Biwa S, Yamamoto S, Kobayashi F and Ohno N 2004 Computational multiple scattering analysis for shear wave propagation in unidirectional composites *Int. J. Solids Struct.* **41** 435–57
- Dirocco A, Molinari S, Stollman A L, Decker A and Yahr M D 1993 MRI abnormalities in Creutzfeldt–Jakob disease *Neuroradiology* **35** 584–5
- Ehman E C, Rossman P J, Kruse S A, Sahakian A V and Glaser K J 2008 Vibration safety limits for magnetic resonance elastography *Phys. Med. Biol.* **53** 925–35
- Glaser K J, Felmlee J P, Manduca A and Ehman R L 2003 Shear stiffness estimation using intravoxel phase dispersion in magnetic resonance elastography *Magn. Reson. Med.* **50** 1256–65
- Glaser K J, Felmlee J P, Manduca A, Kannan Mariappan Y and Ehman R L 2006 Stiffness-weighted magnetic resonance imaging *Magn. Reson. Med.* **55** 59–67
- Graff K F 1991 *Wave Motion in Elastic Solids* (New York: Dover)
- Green M A, Bilston L E and Sinkus R 2008 *In vivo* brain viscoelastic properties measured by magnetic resonance elastography *NMR Biomed* **21** 755–64
- Huwart L *et al* 2008 Magnetic resonance elastography for the noninvasive staging of liver fibrosis *Gastroenterology* **135** 32–40
- Ikuta N, Hirata M, Sasabe F, Negoro K and Morimatsu M 1998 High-signal basal ganglia on T1-weighted images in a patient with Sydenham’s chorea *Neuroradiology* **40** 659–61

- Klatt D, Hamhaber U, Asbach P, Braun J and Sack I 2007 Noninvasive assessment of the rheological behavior of human internal organs using multifrequency MR elastography: a study of brain and liver viscoelasticity *Phys. Med. Biol.* **52** 7281–94
- Kruse S A, Rose G H, Glaser K J, Manduca A, Felmlee J P, Jack C R Jr and Ehman R L 2008 Magnetic resonance elastography of the brain *Neuroimage* **39** 231–7
- Muthupillai R and Ehman R L 1996 Magnetic resonance elastography *Nat. Med.* **2** 601–3
- Papazoglou S, Hamhaber U, Braun J and Sack I 2007 Horizontal shear wave scattering from a nonwelded interface observed by magnetic resonance elastography *Phys. Med. Biol.* **52** 675–84
- Papazoglou S, Hamhaber U, Braun J and Sack I 2008 Algebraic Helmholtz inversion in planar magnetic resonance elastography *Phys. Med. Biol.* **53** 3147–58
- Papazoglou S, Rump J, Braun J and Sack I 2006 Shear-wave group-velocity inversion in MR elastography of human skeletal muscle *Magn. Reson. Med.* **56** 489–97
- Plewes D B, Betty I, Urchuk S N and Soutar I 1995 Visualizing tissue compliance with MR imaging *J. Magn. Reson. Imaging* **5** 733–8
- Rombouts S, Barkhof F, Witter M P and Scheltens P 2000 Unbiased whole-brain analysis of gray matter loss in Alzheimer's disease *Neurosci. Lett.* **285** 231–3
- Rump J, Klatt D, Braun J, Warmuth C and Sack I 2007 Fractional encoding of harmonic motions in MR elastography *Magn. Reson. Med.* **57** 388–95
- Sack I, Beierbach B, Hamhaber U, Klatt D and Braun J 2008 Non-invasive measurement of brain viscoelasticity using magnetic resonance elastography *NMR Biomed.* **21** 265–71
- Samani A, Zubovits J and Plewes D 2007 Elastic moduli of normal and pathological human breast tissues: an inversion-technique-based investigation of 169 samples *Phys. Med. Biol.* **52** 1565–76
- Sarvazyan A P, Skovoroda A R, Emelianov S Y, Fowlkes J B, Pipe J G, Adler R S, Buxton R B and Carson P L 1995 *Biophysical Bases of Elasticity Imaging* vol 21 (New York: Plenum)
- Schroter A, Zerr I, Henkel K, Tschampa H J, Finkenstaedt M and Poser S 2000 Magnetic resonance imaging in the clinical diagnosis of Creutzfeldt-Jakob disease *Arch. Neurol.* **57** 1751–7
- Shenton M E, Dickey C C, Frumin M and McCarley R W 2001 A review of MRI findings in schizophrenia *Schizophr. Res.* **49** 1–52
- Yin M, Rouviere O, Glaser K J and Ehman R L 2008 Diffraction-biased shear wave fields generated with longitudinal magnetic resonance elastography drivers *Magn. Reson. Imaging* **26** 770–80
- Yin M, Talwalkar J A, Glaser K J, Manduca A, Grimm R C, Rossman P J, Fidler J L and Ehman R L 2007 Assessment of hepatic fibrosis with magnetic resonance elastography *Clin. Gastroenterol. Hepatol.* **5** 1207–13, e2